LETTER

doi:10.1038/nature14015

Proton transport through one-atom-thick crystals

S. Hu[1,2], M. Lozada-Hidalgo[1], F. C. Wang[3], A. Mishchenko[1], F. Schedin[2], R. R. Nair[1], E. W. Hill[2], D. W. Boukhvalov[4], M. I. Katsnelson[4], R. A. W. Dryfe[5], I. V. Grigorieva[1], H. A. Wu[3] & A. K. Geim[1,2]

Graphene is increasingly explored as a possible platform for developing novel separation technologies[1–19]. This interest has arisen because it is a maximally thin membrane that, once perforated with atomic accuracy, may allow ultrafast and highly selective sieving of gases, liquids, dissolved ions and other species of interest[2,9–19]. However, a perfect graphene monolayer is impermeable to all atoms and molecules under ambient conditions[1–7]: even hydrogen, the smallest of atoms, is expected to take billions of years to penetrate graphene's dense electronic cloud[3–6]. Only accelerated atoms possess the kinetic energy required to do this[20,21]. The same behaviour might reasonably be expected in the case of other atomically thin crystals[22,23]. Here we report transport and mass spectroscopy measurements which establish that monolayers of graphene and hexagonal boron nitride (hBN) are highly permeable to thermal protons under ambient conditions, whereas no proton transport is detected for thicker crystals such as monolayer molybdenum disulphide, bilayer graphene or multilayer hBN. Protons present an intermediate case between electrons (which can tunnel easily through atomically thin barriers[24]) and atoms, yet our measured transport rates are unexpectedly high[4,5] and raise fundamental questions about the details of the transport process. We see the highest room-temperature proton conductivity with monolayer hBN, for which we measure a resistivity to proton flow of about 10 Ω cm^2 and a low activation energy of about 0.3 electronvolts. At higher temperatures, hBN is outperformed by graphene, the resistivity of which is estimated to fall below 10^{-3} Ω cm^2 above 250 degrees Celsius. Proton transport can be further enhanced by decorating the graphene and hBN membranes with catalytic metal nanoparticles. The high, selective proton conductivity and stability make one-atom-thick crystals promising candidates for use in many hydrogen-based technologies.

We have investigated the possibility of proton transport through monocrystalline membranes made from mono- and few-layer graphene, hBN, and molybdenum disulphide (MoS_2). The two-dimensional (2D) crystals[22,23] were obtained by micromechanical cleavage and then suspended over micrometre-size holes etched through Si wafers (Extended Data Figs 1 and 2). The resulting free-standing membranes were checked for the absence of pinholes and defects and were coated on both sides with Nafion, a polymer with high proton conductivity and negligible electron conductivity[25]. Finally, two proton-injecting PdH_x electrodes[26,27] were deposited onto the Nafion from both sides of the wafer. (See 'Experimental devices' in Methods for a detailed description of the fabrication procedures.) As illustrated in the left inset of Fig. 1a, the 2D crystals effectively serve as atomically thin barriers between two Nafion spaces. For electrical measurements ('Conductance measurements' in Methods), samples were placed in a H–Ar atmosphere at 100% humidity, which ensured high conductivity of the Nafion films[25,26]. Examples of current–voltage characteristics measured for devices incorporating monolayers of graphene, hBN and MoS_2 are shown in Fig. 1a. The measured proton current I varies linearly with bias voltage V, with conductance $S = I/V$ proportional to the membrane area A (Extended Data

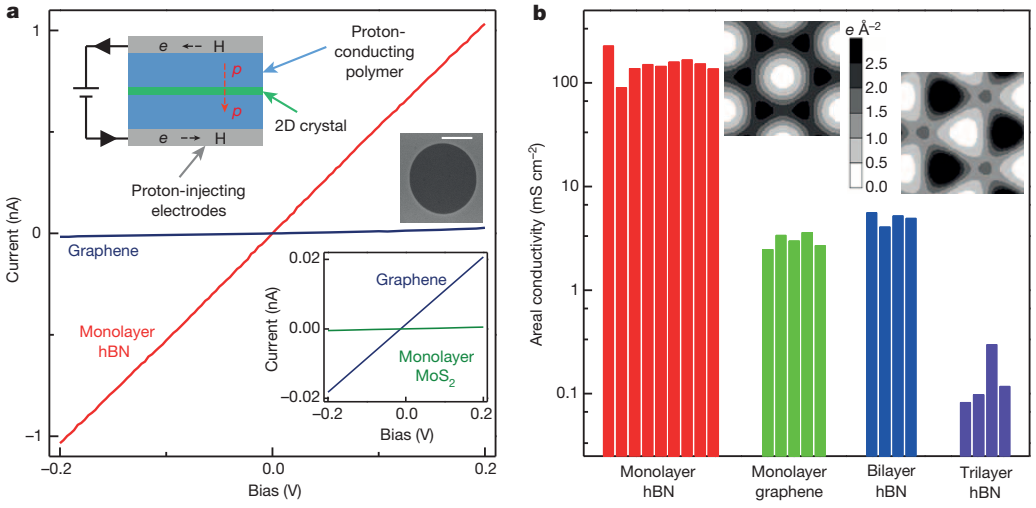

Figure 1 | Proton transport through 2D crystals. a, Examples of I–V characteristics for monolayers of hBN, graphite and MoS_2. The upper inset shows a sketch of the experimental set-up. The middle inset (scale bar, 1 μm) shows an electron micrograph of a typical graphene membrane before the deposition of Nafion. Small (pA) currents observed for MoS_2 membrane devices (lower inset) are due to parasitic parallel conductance. **b**, Histograms for 2D crystals that are found to exhibit measurable proton conductivity. Each bar represents a different sample with a 2 μm-diameter membrane. Insets, charge density (in electrons per Å^2) integrated along the direction perpendicular to graphene (left) and monolayer hBN (right). The white areas are minima at the hexagon centres; the maxima correspond to positions of C, B and N atoms. The measurements were carried out at room temperature (21–23 °C).

[1]School of Physics and Astronomy, The University of Manchester, Manchester M13 9PL, UK. [2]Manchester Centre for Mesoscience and Nanotechnology, The University of Manchester, Manchester M13 9PL, UK. [3]Chinese Academy of Sciences Key Laboratory of Mechanical Behavior and Design of Materials, Department of Modern Mechanics, University of Science and Technology of China, Hefei, Anhui 230027, China. [4]Institute for Molecules and Materials, Radboud University of Nijmegen, 6525 AJ Nijmegen, The Netherlands. [5]School of Chemistry, The University of Manchester, Manchester M13 9PL, UK.

Fig. 3). For 'bare-hole' devices, which were prepared in the same manner but lacked a 2D membrane, S was ~50 times higher than in the presence of monolayer hBN. This confirms that the measured areal conductivity $\sigma = S/A$ is dominated by the 2D crystals, with Nafion contributing only a relatively small series resistance. For devices with thick barriers (for example 100 nm-thick metal or insulating films evaporated between the Nafion spaces), we find a parasitic parallel conductance of ~10 pS caused by leakage currents along silicon nitride surfaces at high humidity (Methods). Within this uncertainty, we could not detect any proton current through monolayer MoS_2, bilayer graphene, four-layer hBN or thicker 2D crystals. The reported behaviour was highly reproducible, as illustrated by statistics in Fig. 1b and Extended Data Fig. 4 for a number of different devices. To further demonstrate the generality of the observed behaviour, we also used a set-up where 2D membranes separate liquid electrolyte cells (containing HCl solutions) instead of Nafion (Methods). We found the same proton conductivities using this electrolyte set-up (Extended Data Fig. 5).

Insight into the difference in permeation through different 2D crystals is gained by considering the electron clouds passed by translocating protons, as shown for graphene and monolayer hBN in the insets of Fig. 1b. Monolayer hBN is more 'porous' than graphene, reflecting that the BN bond is strongly polarized, with valence electrons concentrated around N atoms. The non-permeable MoS_2 consists of three atomic layers containing large atoms, resulting in a much denser electron cloud (Extended Data Fig. 6). The absence of detectable σ for bilayer graphene can be attributed to its AB stacking (the hexagonal rings in each graphene layer are centred on the carbon atoms in the adjacent layer). This results in 'pores' in the electron cloud of one layer being covered by electron density maxima within the adjacent layer. In contrast, the AA′ stacking of hBN (hexagonal rings in different layers are aligned with each other) results in an increase in the integrated electron density with increasing layer number but retains the central pore in the electron cloud even for multilayer hBN membranes.

There is no correlation between proton transport and either the electron transport behaviour or the quality of the 2D crystals. hBN exhibits the highest proton conductivity but is a wide-gap insulator with the highest electron tunnelling barrier[23,24], whereas monolayer MoS_2 shows no discernible proton permeation but is a heavily doped semiconductor with electron-type conductivity[22,28]. And whereas extensive examination using transmission and tunnelling electron microscopy and other techniques ('Absence of atomic-scale defects' in Methods) failed to find even individual pinholes (atomic-scale defects) in graphene and hBN prepared using the same cleavage technique as employed in the present work (see also refs 1, 2, 24 and Extended Data Fig. 7), MoS_2 monolayers contain a high density of sulphur vacancies[29] yet exhibited little proton conductivity. These observations, the high reproducibility of our measurements for different devices, the linear scaling with area A, and the expected changes with increasing layer number all support our conclusion that the measured σ values represent the intrinsic proton conductivity of the studied 2D crystals. (See 'Absence of atomic-scale defects' in Methods for further evidence against the involvement of atomic-scale defects in the observed proton permeation.)

The transport barrier heights E for different 2D crystals are obtained by measuring σ as a function of temperature T (Fig. 2a), revealing that proton conductivities exhibit Arrhenius-type behaviour, $\exp(-E/k_BT)$, where k_B is the Boltzmann constant. We note that the conductivity of Nafion contributes little to the overall value of S, and changes only by a factor of two over the T range examined (Extended Data Fig. 8). The data in Fig. 2a yield $E = 0.78 \pm 0.03$, 0.61 ± 0.04 and 0.3 ± 0.02 eV for graphene, bilayer hBN and monolayer hBN, respectively. Measurements on different devices give values that are reproducible within our experimental accuracy of ~10% (Extended Data Fig. 4). This is consistent with the high reproducibility of σ found for different devices (Fig. 1b) because otherwise different E values should yield hugely different σ values at a given T.

The barrier to proton transport through graphene we have determined is notably lower than the 1.2–2.2 eV found in *ab initio* molecular dynamics simulations and calculations using the climbing-image nudged elastic band method[4–6], which would result in proton conductivities millions of times smaller and undetectable in our experiments. We have reproduced the earlier barrier calculations for graphene and extended them to monolayer hBN ('Theoretical analysis of proton transport through 2D crystals' in Methods), obtaining values of $E = 1.25$–1.40 eV for graphene, in agreement with refs 4, 5, and ~0.7 eV for monolayer hBN. The disagreement between experiment and theory in the absolute value of E is perhaps not surprising given the complex nature of possible transport pathways and the sensitivity of the calculations to pseudopotentials, the exchange correlation functional and so on. The difference might also arise because protons in Nafion and water move along hydrogen bonds[25] rather than in vacuum as assumed by theory so far.

Some applications call for very high proton conductivities, an example being hydrogen fuel cells that require membranes with $\sigma > 1$ S cm^{-2}.

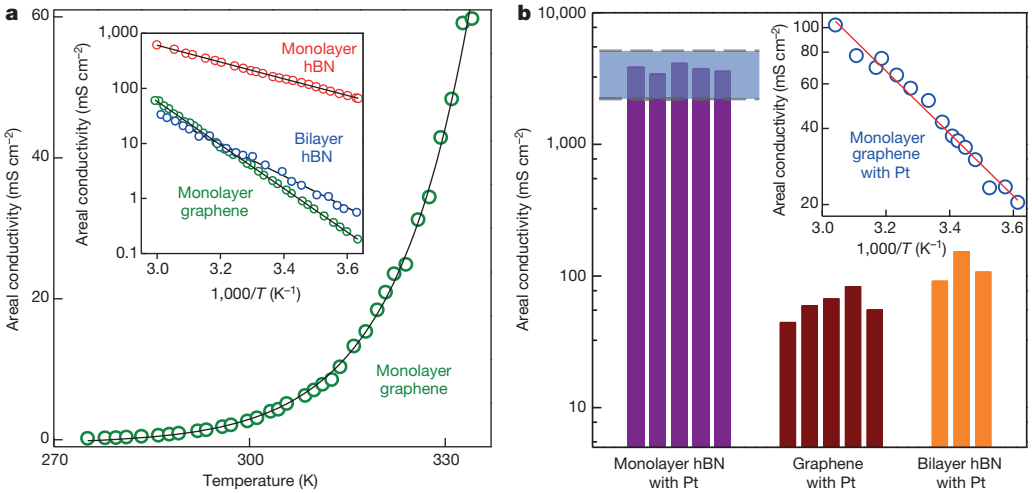

Figure 2 | Proton barrier heights and their catalytic suppression. **a**, Temperature dependences of proton conductivity for 2D crystals. The inset shows $\log(\sigma)$ as a function of T^{-1}. Symbols are experimental data; solid curves are the best fits to the activation dependence. The T range is limited by freezing of water in Nafion, and we normally avoided $T > 60$ °C to prevent accidental damage because of different thermal expansion coefficients. **b**, Proton conductivity of 2D crystals decorated with catalytic nanoparticles. Each bar is a different device. The shaded area shows the conductivity range found for bare-hole devices (Methods). Inset, Arrhenius-type behaviour for graphene decorated with Pt, yielding $E \approx 0.24$ eV. Monolayer hBN decorated with Pt exhibits only a weak T dependence (Extended Data Fig. 8), which indicates that its E becomes comparable to k_BT.

This requirement is met by monolayers of hBN and graphene above 80 and 110 °C, respectively (Fig. 2a). Graphene is known to remain stable in humid oxygen atmospheres up to 400 °C (ref. 30), and extrapolation of its conductivity to an operating temperature of 250 °C, at which it is certainly stable, yields extremely high areal conductivities $\sigma > 10^3$ S cm^{-2}.

Another approach to influencing proton transport through 2D crystals exploits the high affinity of platinum group metals to hydrogen. As shown in Fig. 2b, evaporation of a discontinuous, catalytic layer of Pt or Pd (nominally 1–2 nm thick) onto one of the surfaces of a 2D crystal (see 'Experimental devices' in Methods for fabrication details) resulted in a substantially increased σ. The value of S measured for monolayer hBN became indistinguishable from that of reference bare-hole devices (Fig. 2b), demonstrating that proton permeation (even at room temperature (21–23 °C)) is limited by Nafion's series resistance rather than by passage through the Pt-activated monolayer hBN membrane. Measurements on graphene and bilayer hBN membranes activated with Pt remain little affected by the series resistance and continue to reflect the membranes' intrinsic properties. Temperature-dependent measurements show that Pt reduces the activation energy E by as much as ~0.5 eV (Fig. 2b). This value is in agreement with the ~0.65 eV reduction in E obtained in our simulations of the catalytic effect ('Theoretical analysis of proton transport through 2D crystals' in Methods), which we attribute to attraction of transient protons to Pt (Extended Data Fig. 9). We note that the measurements in Fig. 2b give only a lower limit of ~3 S cm^{-2} for the room-temperature conductivity of catalytically activated monolayer hBN; if this membrane experiences a reduction in E qualitatively similar to that observed for graphene, proton transport across it should be essentially unimpeded.

To demonstrate directly that the applied electric current through our 2D membranes leads to a hydrogen flux, we prepared devices where one of the Nafion–PdH_x contacts is absent and the graphene surface decorated with Pt faces a vacuum chamber equipped with a mass spectrometer (Fig. 3, insets). With either no bias applied between graphene and the remaining PdH_x electrode or a positive bias applied to graphene, we cannot detect any gas leak (including He) between the hydrogen and vacuum chambers (Extended Data Fig. 10). In contrast, applying a negative bias to graphene causes a steady H_2 flux into the vacuum chamber. Its value is determined by the number of protons, I/e (e, elementary charge), passing through the membrane per second. Using the ideal gas law, we find that $F = k_B T(I/2e)$, where the flow rate F is the value measured by the mass spectrometer tuned to molecular hydrogen. The dependence of F on I is shown in Fig. 3 by the solid red line, in excellent agreement with the experiment.

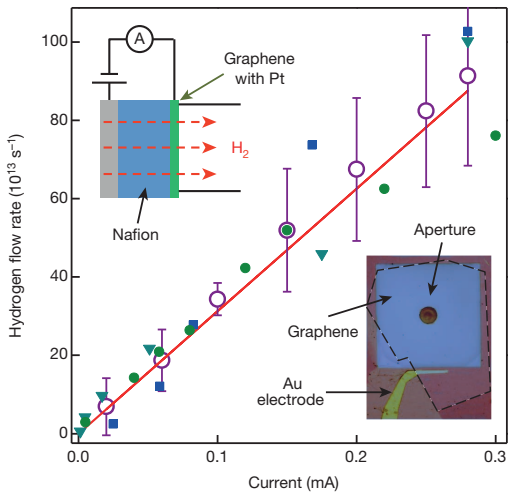

Figure 3 | Current-controlled hydrogen flux. Top inset, sketch of our mass spectrometry experiment. Monolayer graphene decorated with Pt nanoparticles separates a vacuum chamber from the Nafion–PdH_x electrode placed under the same H_2/H_2O conditions as described in 'Conductance measurements' in Methods. Protons penetrate the membrane and recombine into molecular hydrogen. The hydrogen flux (main plot) is detected by a mass spectrometer (Methods). Different symbols refer to different devices. Error bars indicate characteristic fluctuations in the measured signal and the red line is the theoretically expected flow rate. Bottom inset, optical image of one of the devices. Graphene (outlined by the dashed lines) seals a circular aperture 50 μm in diameter etched through the SiN_x membrane (Extended Data Fig. 1). Nafion is underneath the graphene and SiN_x membranes.

Taken together, our observations establish that monolayers of graphene and hBN constitute a class of proton conductors that raise intriguing questions about the transfer of subatomic particles through atomically thin electron clouds. Moreover, the high proton conductivity, chemical and thermal stability, and impermeability to H_2, water and methanol make these membranes attractive candidates for use in various hydrogen technologies. For example, they might be developed into proton membranes for use in fuel cells to solve the problem of fuel crossover and poisoning currently challenging this technology. The demonstrated ability of these membranes to act as a current-controlled source of hydrogen is also appealing for its simplicity and, once large-area graphene and hBN films become commercially available, might be used to extract hydrogen from gas mixtures or air.

Online Content Methods, along with any additional Extended Data display items and Source Data, are available in the online version of the paper; references unique to these sections appear only in the online paper.

Received 25 August; accepted 23 October 2014.
Published online 26 November 2014.

1. Bunch, J. S. *et al.* Impermeable atomic membranes from graphene sheets. *Nano Lett.* **8,** 2458–2462 (2008).
2. Koenig, S. P., Wang, L., Pellegrino, J. & Bunch, J. S. Selective molecular sieving through porous graphene. *Nature Nanotechnol.* **7,** 728–732 (2012).
3. Leenaerts, O., Partoens, B. & Peeters, F. M. Graphene: a perfect nanoballoon. *Appl. Phys. Lett.* **93,** 193107 (2008).
4. Wang, W. L. & Kaxiras, E. Graphene hydrate: theoretical prediction of a new insulating form of graphene. *New J. Phys.* **12,** 125012 (2010).
5. Miao, M., Nardelli, M. B., Wang, Q. & Liu, Y. First principles study of the permeability of graphene to hydrogen atoms. *Phys. Chem. Chem. Phys.* **15,** 16132–16137 (2013).
6. Tsetseris, L. & Pantelides, S. T. Graphene: an impermeable or selectively permeable membrane for atomic species? *Carbon* **67,** 58–63 (2014).
7. Berry, V. Impermeability of graphene and its applications. *Carbon* **62,** 1–10 (2013).
8. Yuan, W., Chen, J. & Shi, G. Nanoporous graphene materials. *Mater. Today* **17,** 77–85 (2014).
9. Sint, K., Wang, B. & Král, P. Selective ion passage through functionalized graphene nanopores. *J. Am. Chem. Soc.* **130,** 16448–16449 (2008).
10. Jiang, D. E., Cooper, V. R. & Dai, S. Porous graphene as the ultimate membrane for gas separation. *Nano Lett.* **9,** 4019–4024 (2009).
11. Garaj, S. *et al.* Graphene as a subnanometre trans-electrode membrane. *Nature* **467,** 190–193 (2010).
12. O'Hern, S. C. *et al.* Selective molecular transport through intrinsic defects in a single layer of CVD graphene. *ACS Nano* **6,** 10130–10138 (2012).
13. Cohen-Tanugi, D. & Grossman, J. C. Water desalination across nanoporous graphene. *Nano Lett.* **12,** 3602–3608 (2012).
14. Kim, H. W. *et al.* Selective gas transport through few-layered graphene and graphene oxide membranes. *Science* **342,** 91–95 (2013).
15. Li, H. *et al.* Ultrathin, molecular-sieving graphene oxide membranes for selective hydrogen separation. *Science* **342,** 95–98 (2013).
16. Konatham, D., Yu, J., Ho, T. A. & Striolo, A. Simulation insights for graphene-based water desalination membranes. *Langmuir* **29,** 11884–11897 (2013).
17. Celebi, K. *et al.* Ultimate permeation across atomically thin porous graphene. *Science* **344,** 289–292 (2014).
18. O'Hern, S. C. *et al.* Selective ionic transport through tunable subnanometer pores in single-layer graphene membranes. *Nano Lett.* **14,** 1234–1241 (2014).
19. Sun, C. *et al.* Mechanisms of molecular permeation through nanoporous graphene membranes. *Langmuir* **30,** 675–682 (2014).
20. Stolyarova, E. *et al.* Observation of graphene bubbles and effective mass transport under graphene films. *Nano Lett.* **9,** 332–337 (2009).
21. Banhart, F., Kotakoski, J. & Krasheninnikov, A. V. Structural defects in graphene. *ACS Nano* **5,** 26–41 (2011).
22. Novoselov, K. S. *et al.* Two-dimensional atomic crystals. *Proc. Natl Acad. Sci. USA* **102,** 10451–10453 (2005).
23. Geim, A. K. & Grigorieva, I. V. Van der Waals heterostructures. *Nature* **499,** 419–425 (2013).
24. Britnell, L. *et al.* Electron tunneling through ultrathin boron nitride crystalline barriers. *Nano Lett.* **12,** 1707–1710 (2012).
25. Mauritz, K. & Moore, R. B. State of understanding of Nafion. *Chem. Rev.* **104,** 4535–4586 (2004).

26. Morgan, H., Pethig, R. & Stevens, G. T. A proton-injecting technique for the measurement of hydration-dependent protonic conductivity. *J. Phys. E* **19,** 80–82 (1986).
27. Zhong, C. *et al.* A polysaccharide bioprotonic field-effect transistor. *Nature Commun.* **2,** 476 (2011).
28. Radisavljevic, B., Radenovic, A., Brivio, J., Giacometti, V. & Kis, A. Single-layer MoS_2 transistors. *Nature Nanotechnol.* **6,** 147–150 (2011).
29. Qiu, H. *et al.* Hopping transport through defect-induced localized states in molybdenum disulphide. *Nature Commun.* **4,** 2642 (2013).
30. Liu, L. *et al.* Graphene oxidation: thickness-dependent etching and strong chemical doping. *Nano Lett.* **8,** 1965–1970 (2008).

Acknowledgements This work was supported by the European Research Council, the Royal Society, the Office of Naval Research, the Air Force Office of Scientific Research and the National Science Foundation of China. M.L.-H. acknowledges a PhD studentship provided by the Consejo Nacional de Ciencia y Tecnología (Mexico).

Author Contributions A.K.G. designed the project and directed it with help from S.H. and M.L.-H., who fabricated devices, performed measurements and carried out data analyses. H.A.W. and F.C.W. provided theoretical support. M.L.-H., H.A.W., I.V.G. and A.K.G. wrote the manuscript. All authors contributed to discussions.

Author Information Reprints and permissions information is available at www.nature.com/reprints. The authors declare no competing financial interests. Readers are welcome to comment on the online version of the paper. Correspondence and requests for materials should be addressed to M.L.-H. (marcelo.lozadahidalgo@manchester.ac.uk) or H.A.W. (wuha@ustc.edu.cn).

METHODS

Experimental devices. Extended Data Fig. 1 explains our microfabrication procedures. We start with preparing free-standing silicon nitride (SiN_x) membranes from commercially available Si wafers coated on both sides with 500 nm of SiN_x. Reactive ion etching (RIE) is employed to remove a 1×1 mm^2 section from one of the SiN_x layers (steps 1 and 2 in Extended Data Fig. 1). The wafer is then exposed to a KOH solution that etches away Si and leaves a free-standing SiN_x membrane of typically 300×300 μm^2 in size (step 3). During step 4, a circular hole is drilled by RIE through the SiN_x membrane using the same procedures as in steps 1 and 2. Next a 2D crystal (graphene, hBN or MoS_2) is prepared by standard micromechanical exfoliation[22] and transferred on top of the membrane using either the wet or dry technique[31,32] to cover the aperture in the SiN_x (step 5). We used hBN crystals commercially supplied by HQ Graphene.

After step 5, the suspended membranes could be examined for their integrity and quality in a scanning electron microscope (SEM). Pristine 2D crystals give little SEM contrast, and it requires some contamination to notice 2D membranes on top of the holes. Contamination can be accidental or induced by the electron beam (Extended Data Fig. 2). If cracks or tears are present, they are clearly seen as darker areas. No such defects could be found in many membranes we visualized in SEM. Occasional cracks such as in Extended Data Fig. 2b were only observed if introduced deliberately or a profound mistake was made during handling procedures. We did not notice any effect of SEM imaging on proton transport but nevertheless avoided prolonged SEM exposures. Because cracks were exceptionally rare, we did not find it necessary to image all the reported devices using SEM.

The fabrication of devices for electrical measurements continues with the deposition of a proton-conducting polymer layer. A Nafion solution (5%, 1,100 equiv. wt) is drop-cast on both sides of a suspended 2D membrane (step 6 in Extended Data Fig. 1). Finally, palladium hydride (PdH_x) electrodes are mechanically attached to the Nafion layers. To synthesize these electrodes, a 25 μm-thick Pd foil is left overnight in a saturated hydrogen-donating solution following the procedure of ref. 33. This leads to atomic hydrogen being absorbed into the crystal lattice of Pd, turning it into PdH_x. The resulting devices are placed in a water-saturated environment at 130 °C to crosslink the polymer and improve electrical contacts.

The described experimental design is optimized to take into account the following considerations. First, electric currents in Nafion are known to be carried exclusively by protons that hop between immobile sulphonate groups[25]. Nafion is not conductive for electrons, which can be demonstrated directly by, for example, inserting a gold film across a Nafion conductor, which breaks down the electrical connectivity. Accordingly, protons are the only mobile species that can pass between our PdH_x electrodes. Second, PdH_x is widely used as a proton-injecting material that converts an electron (e) flow into a proton (p) one by the following process: $PdH_x \rightarrow Pd + xp + xe$ (refs 26, 27, 34). This property, combined with the large area of our electrodes (relative to the membrane area A), makes the contact resistance between Nafion and PdH_x negligible such that the circuit conductance in our experiments is limited by either the 2D crystals or, in their absence, the Nafion constriction of diameter D.

For the catalytically activated measurements, 1–2 nm of Pt were deposited by e-beam evaporation directly onto the suspended membrane to form a discontinuous film before the Nafion was deposited. Thicker, continuous films were found to block proton currents. This blocking could be witnessed as the appearance of numerous hydrogen bubbles under the Pt after passage of an electric current. Typically, our Pt films resulted in ~80% area coverage, which reduced the effective area for proton transport accordingly, as found by depositing such Pt films between the Nafion layers, without 2D membranes (see below). Pd was found to be less blocking, and Pd films up to several nanometres thick did not notably impede the proton flow. Otherwise, both Pd and Pt resulted in similar enhancement of proton transport through 2D crystals.

Conductance measurements. The devices described above were placed inside a metal chamber filled with a forming gas (10% H_2 in Ar) and containing some liquid water to provide 100% relative humidity. Devices were bonded with gold wires, and I–V curves were recorded using d.c. measurements (Keithley 2636A). We typically varied the voltage in the range of −1 to 1 V at sweep rates up to 0.5 V min^{-1}. We avoided higher voltages because I–V characteristics could become nonlinear and membranes could delaminate as a result of bubble formation. The reported I–V curves were non-hysteretic and highly reproducible. The devices were stable for several weeks if not allowed to dry out.

To characterize our experimental set-up, we first measured leakage currents in the absence of a proton-conductive path. To this end, two metallic contacts were placed on opposite surfaces of a piece of a fresh Si/SiN_x wafer and I–V characteristics were measured under the same humid conditions as above. A conductance of the order of ~5 pS was normally registered. We also used fully processed devices and then mechanically removed the Nafion film and electrodes. In the latter case, the parasitic conductance was slightly (a factor of two) higher, which is probably due to a processing and polymer residue left on SiN_x. In principle, it would be possible to reduce the leakage currents by using, for example, separate chambers on opposite sides of the Si wafer[11], but the observed parasitic conductance was deemed small enough for the purpose of the present work.

As a reference, we studied the conductivity of bare-hole devices that were prepared in exactly the same manner as our membrane devices but without a 2D crystal covering the aperture (step 5 in Extended Data Fig. 1 was omitted). Extended Data Fig. 3a shows the conductance of such devices as a function of their diameter D. Within the experimental scatter, conductance S increases linearly with D, in agreement with Maxwell's formula[35]: $S = \sigma_N D$. The latter is derived by solving Laplace's equation for two semi-spaces that have conductivity σ_N and are connected by a tube with D much larger than its length d. In our case, $d = 500$ nm and the condition is satisfied, except possibly by the smallest membranes with $D = 2$ μm.

From the dependence shown in Extended Data Fig. 3a, we can estimate the bulk conductivity of our Nafion films as ~1 mS cm^{-1}. As shown in the main text, Nafion's conductivity did not limit our measurements of proton transport through 2D crystals, except for the case of catalytically activated monolayer hBN. Nonetheless, we note that the found σ_N value is two orders of magnitude smaller than values achievable for highest-quality Nafion[36]. There are two reasons for this. First, solution-cast Nafion like that used in our experiments is known to be typically one order of magnitude lower in conductivity than the highest-quality Nafion[37,38]. Second, to achieve the highest conductivity, Nafion is normally pre-treated by boiling in H_2O_2 and H_2SO_4 for several hours[36–38]. When this procedure was used, our Nafion films indeed increased their conductivity by a factor of ten, reaching the standard values for solution-cast Nafion of ~10 mS cm^{-1}. Unfortunately, this harsh treatment destroyed our membrane devices, with the Nafion delaminating from SiN_x, and so could not be used. Proton concentrations can be estimated[39] from σ_N and, for our films, are expected to be ~0.1 M.

For consistency, most of the 2D membranes reported in the main text were 2 μm in diameter. However, we studied many other membranes with D ranging from 1 to 50 μm. Their conductances are found to scale linearly with the aperture area A. Extended Data Fig. 3b shows this for ten monolayer hBN devices with D between 1 and 4 μm. Within the experimental scatter for devices of the same D, the conductance increases linearly with A, in agreement with general expectations. The same scaling was also observed for graphene membranes.

Reproducibility. Figures 1b and 2b show that our measurements of σ were highly reproducible for different devices of nominally the same size. The scatter in σ can be attributed to accidental contamination that blocks proton currents through parts of the 2D membranes. Further evidence of little variation in σ for different devices is provided by the correct scaling of σ with membrane area (Extended Data Fig. 3b). It is important to emphasize that, because of the exponential dependence of σ on T, the high reproducibility of σ at room temperature implies that the activation energies E also cannot differ much for different devices. Nonetheless, to show directly that E is device independent, Extended Data Fig. 4 plots $\sigma(T)$ for three bilayer hBN membranes. The best fits respectively yield $E = 0.65$, 0.59 and 0.57 eV. These values fall within the uncertainty interval (0.61 ± 0.04 eV) stated for bilayer hBN in the main text. Furthermore, the inset of Extended Data Fig. 4 compares $\sigma(T)$ for the device shown in Fig. 2a with data obtained for three other graphene membranes. These devices failed during measurements, presumably owing to mechanical strain induced by changes in T. However, the data acquired before the devices broke show that all the membranes have the same activation energy.

Although Nafion was the material of choice in this work owing to its stability and convenience of handling, to prove the generality of our results we also investigated the proton conductivity of 2D crystals when they were immersed in water. For these experiments, 2D membranes were fabricated in the same way as described previously, but, instead of covering the 2D crystals with Nafion, they were used to separate two reservoirs containing liquid electrolytes (Extended Data Fig. 5). Typical I–V characteristics recorded for membranes made from mono-, bi-, and tri-layer hBN in the liquid-cell set-up are presented in Extended Data Fig. 5a. They were recorded using chronoamperometry, and the values shown in the figure correspond to stable currents. The current response was symmetric for positive and negative biases. For devices prepared in the same manner but without a 2D membrane, the conductance S was $>10^3$ times higher than in the presence of monolayer hBN, which ensured that the 2D crystals limited the proton current in the liquid-cell set-up. As in the case of Nafion, we also found a parasitic parallel conductance, but it was somewhat higher (~20 pS) because of the liquid environment. Although it should be possible[11] to reduce the leakage current in the liquid-cell set-up, we find the present accuracy sufficient for our objectives. Within this uncertainty, we could not detect any proton current through either trilayer hBN or, as for the Nafion set-up, monolayer MoS_2, bilayer graphene or any thicker 2D crystals. The observed proton conductivity was highly reproducible for different devices, as shown by the statistics in Extended Data Fig. 5b. Most importantly, the measured proton conductivities agree well with the values found using Nafion as the proton-conducting

medium (compare Fig. 1b with Extended Data Fig. 5b). We note that the devices used in the liquid-cell experiments were more fragile than those in the Nafion experiments and survived for shorter times because of the lack of mechanical support. Accordingly, we focused in our present work on Nafion devices.

Absence of atomic-scale defects. As discussed above, visual inspection of membranes using SEM can reliably rule out holes and cracks with sizes down to ~10 nm (Extended Data Fig. 2b). However, SEM cannot resolve nanometre- or atomic-scale defects, and other techniques are necessary to rule out pinholes of these sizes. As already mentioned in the main text, no such defects have ever been reported for pristine graphene obtained by micromechanical cleavage in numerous transmission electron microscopy and scanning tunnelling microscopy studies over many years. To add to this argument in the case of our particular membranes, we used Raman spectroscopy, which is known to be extremely sensitive to atomic-scale defects in graphene. The intensity of the D peak (~1,350 cm^{-1}) provides a good estimate of their concentration. Importantly, atomic-scale defects can be not only vacancies or larger pinholes but also adatoms that should not allow protons through. Therefore, the D peak provides the upper limit on the concentration of pinholes. Despite our efforts, we could not discern any D peak in our graphene membranes[40]. These measurements set a limit on possible pinhole densities as ~10^8 cm^{-2}, or one defect per μm^2 (ref. 40). Furthermore, such a low density of defects in graphene (including adatoms) is in stark contrast with a high density (~10^{13} cm^{-2}) of sulphur vacancies found in mechanically cleaved MoS_2 (ref. 29). Nevertheless, no proton current could be detected in our MoS_2 membranes. If we assume each vacancy to provide a hole of ~1 Å in size, the expected ~10^5 vacancies present in our typical MoS_2 membranes would provide an effective opening ~30 nm in diameter. Using the results of Extended Data Fig. 3a, this is expected to lead to a conductance of ~3 nS, which is >100 times larger than the limit on σ set by our measurements for monolayer MoS_2. This indicates that individual vacancies may increase the proton conductance much less than their classical diameter suggests. This conclusion is confirmed by using devices made from graphene and hBN monolayers, which were grown by chemical vapour deposition (CVD). Such CVD materials are known to contain many atomic-scale defects, as evidenced, for example, by a strong D peak. Nevertheless, CVD membranes had the same proton conductivity as that found for cleaved monolayers. This unambiguously shows that, even if a few atomic-scale pinholes were present in cleaved 2D crystals, they could not noticeably contribute to the reported σ.

To strengthen the above arguments further, we tried to rule out the presence of even individual vacancies in our cleaved graphene and hBN devices. The most sensitive technique known to detect pinholes is arguably the measurement of gas leakage from small pressurized volumes[1,2]. To this end, a microcavity typically ~1 μm^3 in size is etched in a Si/SiO_2 wafer, sealed with graphene or hBN and then pressurized. If the pressure inside the microcavity is higher than that outside, the membrane bulges upwards; if it is lower, downwards. Changes in pressure can be monitored by measuring the height of the bulge as a function of time using atomic force microscopy (AFM). If there are no holes in the membrane, the gas leaks out slowly along the SiO_2 layer: it typically takes many hours until the pressures inside and outside the microcavity equalize[1]. However, the presence of even a single atomic-scale hole, through which atoms can effuse, allows the pressure to equalize in less than a second[2]. Following the procedures reported previously[1,2], we prepared microcavities in a Si/SiO_2 wafer and sealed them with cleaved monolayer graphene. The microcavities were placed inside a chamber filled with Ar at 200 kPa for typically four days to gradually pressurize them. After taking the devices out, the membranes were found to bulge upwards. Extended Data Fig. 7 shows the deflation of such microballoons with time. In agreement with the previous report[1], the Ar leak rates were found to be ~10^3 atoms per second. If one or a few atomic-scale holes were introduced by, for example, ultraviolet chemical etching, the leak rate increased by many orders of magnitude, leading to practically instantaneous deflation[2]. This shows again that no atomic-scale defects were present in our membranes obtained by mechanical cleavage.

Nafion-limited conductivity. We have reported in the main text that the proton conductivity of catalytically activated monolayer hBN is so high that the series resistance of Nafion becomes the limiting factor in our measurements. This observation is further illustrated in Extended Data Fig. 8 by comparing T dependences for different devices in which Nafion was the limiting factor (bare-hole, Nafion/Pt/Nafion and hBN-with-Pt devices). Consistent with the small activation energy for proton transport in Nafion (<0.02 eV; ref. 36), we found that temperature effects in all such devices are small over the entire T range (Extended Data Fig. 8). The non-monotonic T dependence for the devices with a Pt layer remains to be understood, but we note that Nafion often exhibits similar non-monotonic behaviour[41] at higher T, beyond the temperature range shown in Extended Data Fig. 8. We speculate that the Pt activation shifts this peak to lower T. Importantly, the influence of Pt on local conductivity in the Nafion constriction is approximately the same independently of whether or not an hBN membrane is present. This confirms that the proton conductivity of Pt-activated hBN is so high that it becomes unmeasurable in our experiments. It would require membranes with much larger D to determine σ for catalytically activated hBN.

Theoretical analysis of proton transport through 2D crystals. It is possible to understand the differences that we find in σ by considering the electron clouds created by different 2D crystals. These clouds impede the passage of protons through 2D membranes. In addition to the plots of the electron density in Fig. 1b, Extended Data Fig. 6 shows similar plots of the electron clouds with superimposed positions of C, B and N atoms using the ball-and-stick model of the graphene and hBN crystal lattices. In addition, Extended Data Fig. 6 plots the electron density for monolayer MoS_2 consisting of a monolayer of Mo atoms sandwiched between two monolayers of sulphur. One can immediately see that the latter cloud is much denser than those of monolayer hBN and graphene, which qualitatively explains the absence of proton transport through MoS_2 monolayers.

For quantitative analysis, let us first note that proton permeation through graphene has previously been studied[4–6] using both *ab initio* molecular dynamics (AIMD) simulations and the climbing-image nudged elastic band (CI-NEB) method. These studies have provided estimates for the proton barrier E created by graphene, which range from ~1.17 to 2.21 eV (refs 4–6). We reproduced those results for the case of graphene and extended them to monolayer hBN. Our simulations were performed using the CP2K package[42] with the Pade exchange correlation functional form[43]. The energy cut-off of plane-wave expansions was 380 Ry, and we used the double-ζ valence basis with one set of polarization functions[44] and the Goedecker–Teter–Hutter pseudopotentials[43]. In the first approach, the bombardment of graphene and monolayer hBN with protons of varying kinetic energy was simulated using AIMD in the NVE ensemble (that is, the number of atoms, the volume and the energy are assumed to be constant). The barrier was estimated to be the minimum kinetic energy necessary for proton transfer. The AIMD simulations have yielded E for graphene of between 1.30 and 1.40 eV, in good agreement with refs 4, 5.

In the second (CI-NEB) approach, we calculated the energy for various configurations (usually referred to as 'images'), which correspond to different distances between a proton and a 2D membrane[45]. This provided a series of images for a proton approaching the membrane. The energy was then minimized over obtained images and plotted as a function of proton–crystal distance. The barrier E was estimated using the differential height of such energy profiles. Extended Data Fig. 9 shows examples of these profiles for graphene and monolayer hBN. From the CI-NEB calculations, we estimate the proton barriers to be 1.26 and 0.68 eV for graphene and monolayer hBN, respectively, in agreement with our AIMD results. Finally, to model the effect of Pt on proton transport, we again used AIMD simulations. To this end, four Pt atoms were placed at a fixed distance of 4 Å from the graphene membrane and the bombardment with protons was simulated as described above (Extended Data Figs 9c, d). The addition of the Pt atoms resulted in a significant reduction of the graphene barrier to ~0.6 eV; that is, by a factor of two. The absolute value of the reduction in the barrier height is in agreement with the experiment.

Our measurements also show that I–V characteristics remain linear over a wide range of biases V (up to 1.5 V in the case of Extended Data Fig. 5a). This observation is surprising because the voltage drop across the proton barrier becomes comparable to the barrier height divided by the charge of proton, E/e. Under these circumstances, one intuitively expects a considerable increase in the barrier transparency and strongly nonlinear I–V characteristics, as happens in the case of electron tunnelling. To understand the observed linear behaviour, we modelled our experimental situation using both AIMD and CI-NEB simulations. Additional accelerating fields of up to 1 V nm^{-1} were applied across a graphene sheet. We have found that E changes little, by only ~15 meV for the highest simulated field. Because of inevitable screening by mobile ions, we expect significantly lower electric fields in our experiments than 1 V nm^{-1}, which implies that E changes by much less than k_BT. The low sensitivity of E with respect to V is in agreement with the linear I–V characteristics observed experimentally, but the physical origin of this behaviour remains to be understood. Tentatively, we attribute it to the following: applied voltage not only accelerates protons but also polarizes the electron clouds of 2D crystals, which in turn leads to significant deceleration of protons.

Detection of proton flow by mass spectrometry. To illustrate that the electric current through our 2D membranes is carried by hydrogen ions, we used an alternative set-up described in the main text and shown in more detail in Extended Data Fig. 10a. Protons transferring through graphene are collected at a catalyst Pt layer where they recombine to form molecular hydrogen: $2p + 2e \rightarrow H_2$. The hydrogen flux is then measured with a mass spectrometer (Inficon UL200). Because the electric current I is defined by the number of protons passing through the graphene membrane, the hydrogen flow F is directly related to the passing current I, with no fitting parameters (see the main text).

For this particular experiment, the membrane devices were made as large as possible (50 μm in diameter) to increase the hydrogen flux to values that could be detected using our mass spectrometer. To collect the electric current at the graphene

membrane, a metallic contact (100 nm Au/5 nm Cr) was fabricated next to the SiN_x aperture, before graphene was transferred on top, to cover both aperture and contact (right inset of Fig. 3). This side of the Si wafer (with graphene on top) was then decorated with 1–2 nm of Pt to increase the proton flux. The opposite face of the graphene membrane was covered with Nafion and connected to a PdH_x electrode in the way described above. The resulting device on the Si wafer was glued with epoxy to a perforated Cu foil that was clamped between two O rings to separate two chambers: one filled with a gas and the other connected to the mass spectrometer (Extended Data Fig. 10a). First, we always checked for possible leaks by filling the gas chamber with helium at atmospheric pressure. No He leak could be detected above background readings of the spectrometer ($\sim 10^{-8}$ bar cm^3 s^{-1}). Then the chamber was filled with our standard gas mixture (10% H_2 in Ar at 1 bar and at 100% humidity). No hydrogen flux could be detected without applying negative bias to the graphene. By applying such a bias a controllable flow of H_2 at a level of $\sim 10^{-5}$ bar cm^3 s^{-1} or $\sim 10^{14}$ hydrogen molecules per second was readily detected (Extended Data Fig. 10b). This figure shows the hydrogen flow rates F as a function of time for one of our devices using negative biases from 0 to 20 V. When cycling back from 20 to 0 V, the curves retraced themselves, indicating that the membrane was undamaged during the measurements.

Atomic hydrogen is highly unstable with respect to its molecular form, and it is most likely that the conversion into molecular hydrogen takes places at the surface of Pt rather than in the vacuum chamber. Accordingly, the Pt layer has to be discontinuous to let hydrogen escape. For continuous coverage (>5 nm of Pt), we observed formation of small hydrogen bubbles that grew as we increased the amount of electric charge passed through the circuit. The largest bubbles eventually burst. It is also instructive to mention the case in which a continuous Au films was evaporated on top of the above devices (already containing a discontinuous Pt layer). We found that a bias applied across such devices resulted in the formation of large bubbles at the interface between the graphene and the metal film. The bubbles could burst and sometimes damaged the membrane. This precluded the use of continuous metal films for the mass spectrometry experiment. The same bubbling effect was observed for hBN membranes covered with a Pt film providing continuity of the electrical circuit for insulating hBN. These observations serve as yet another indication of proton transfer through graphene and hBN membranes. However, no bubbles could be observed for thicker 2D crystals, which again proves their impermeability to protons.

31. Nair, R. R. *et al.* Graphene as a transparent conductive support for studying biological molecules by transmission electron microscopy. *Appl. Phys. Lett.* **97,** 153102 (2010).
32. Kretinin, A. V. *et al.* Electronic properties of graphene encapsulated with different two-dimensional atomic crystals. *Nano Lett.* **14,** 3270–3276 (2014).
33. Murphy, D. W. *et al.* A new route to metal hydrides. *Chem. Mater.* **5,** 767–769 (1993).
34. Schuldiner, S., Castellan, G. W. & Hoare, J. P. Electrochemical behavior of the palladium-hydrogen system. I. Potential-determining mechanisms. *J. Chem. Phys.* **28,** 16–19 (1958).
35. Agraït, N., Yeyati, A. L. & van Ruitenbeek, J. M. Quantum properties of atomic-sized conductors. *Phys. Rep.* **377,** 81–279 (2003).
36. Sone, Y., Ekdunge, P. & Simonsson, D. Proton conductivity of Nafion 117 as measured by a four electrode AC impedance method. *J. Electrochem. Soc.* **143,** 1254–1259 (1996).
37. Silva, R., De Francesco, M. & Pozio, A. Solution-cast Nafion® ionomer membranes: preparation and characterization. *Electrochim. Acta* **49,** 3211–3219 (2004).
38. Deluca, N. & Elabd, Y. Nafion/poly(vinyl alcohol) blends: effect of composition and annealing temperature on transport properties. *J. Membr. Sci.* **282,** 217–224 (2006).
39. Spry, D. B. & Fayer, M. D. Proton transfer and proton concentrations in protonated Nafion fuel cell membranes. *J. Phys. Chem. B* **113,** 10210–10221 (2009).
40. Alberti, G., Casciola, M., Massinelli, L. & Bauer, B. Polymeric proton conducting membranes for medium temperature fuel cells (110–160 °C). *J. Membr. Sci.* **185,** 73–81 (2001).
41. Ni, Z. H. *et al.* On resonant scatterers as a factor limiting carrier mobility in graphene. *Nano Lett.* **10,** 3868–3872 (2010).
42. VandeVondele, J. *et al.* Quickstep: fast and accurate density functional calculations using a mixed Gaussian and plane waves approach. *Comput. Phys. Commun.* **167,** 103–128 (2005).
43. Goedecker, S., Teter, M. & Hutter, J. Separable dual-space Gaussian pseudopotentials. *Phys. Rev. B* **54,** 1703–1710 (1996).
44. VandeVondele, J. & Hutter, J. Gaussian basis sets for accurate calculations on molecular systems in gas and condensed phases. *J. Chem. Phys.* **127,** 114105 (2007).
45. Henkelman, G., Uberuaga, B. P. & Jónsson, H. A climbing image nudged elastic band method for finding saddle points and minimum energy paths. *J. Chem. Phys.* **113,** 9901–9904 (2000).

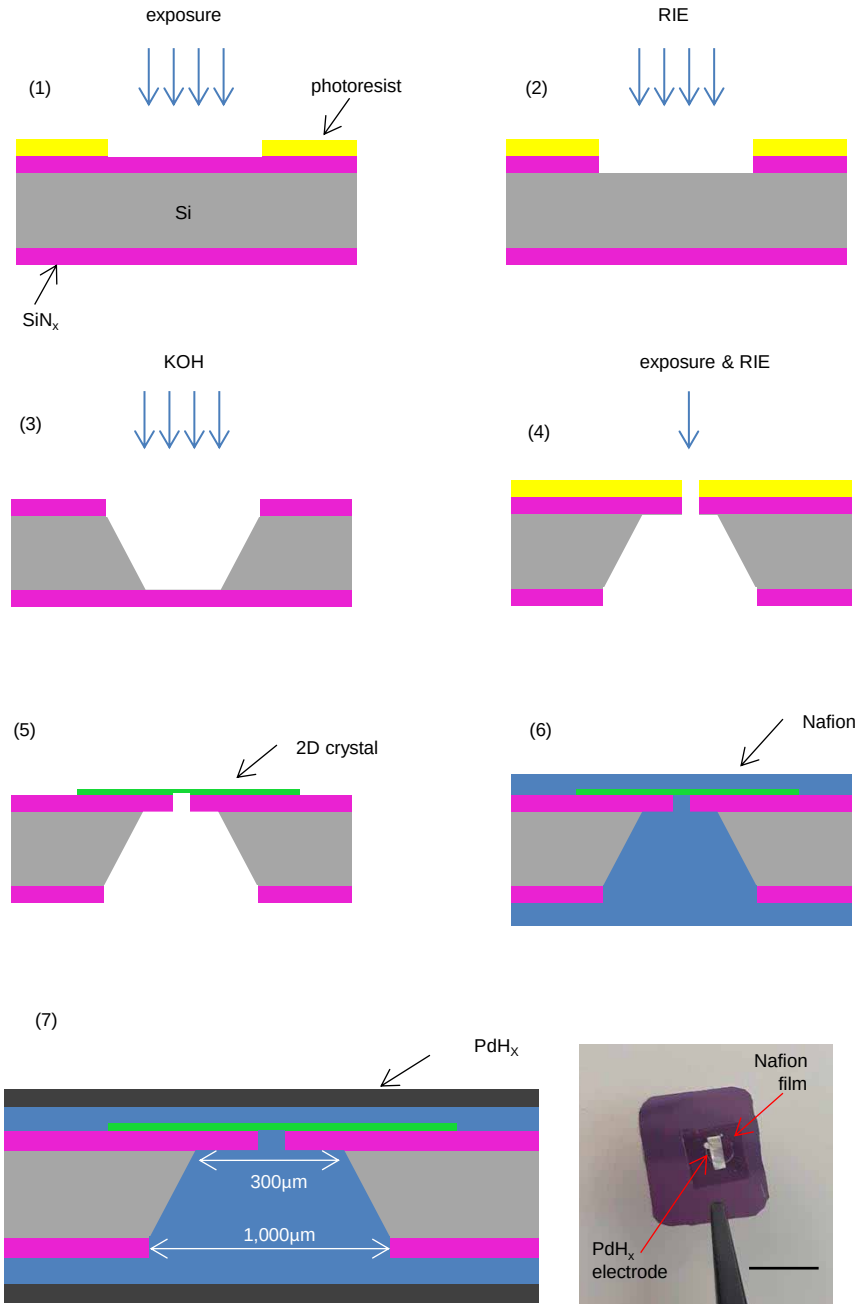

Extended Data Figure 1 | Microfabrication process flow. (1) An etch mask is made by photolithography. (2) RIE is used to remove the exposed SiN_x layer. (3) Si underneath is etched away by wet chemistry. (4) By repeating steps 1 and 2, a hole is drilled through the membrane. (5) The 2D crystal is transferred to cover the etched hole. (6) Nafion is deposited on both sides of the wafer. (7) PdH_x electrodes are attached. Bottom right, optical photo of the final device. Scale bar, 1 cm.

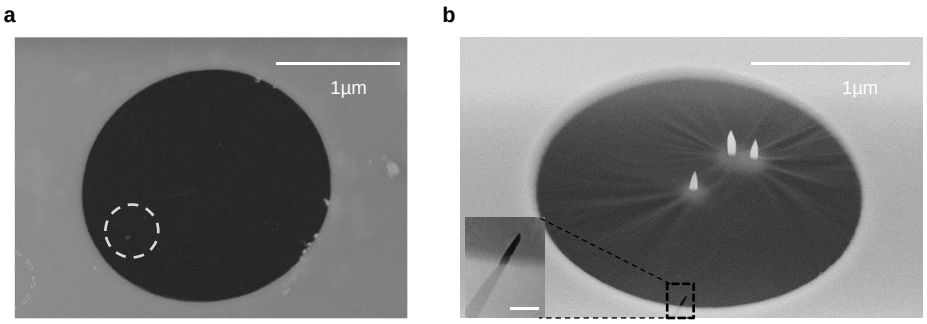

Extended Data Figure 2 | SEM images of suspended 2D crystals. **a**, Monolayer graphene with some accidental contamination. One of the particles away from the edge is marked with a white circle. **b**, Suspended graphene with pillars of hydrocarbon contamination intentionally induced by a focused electron beam. The inset shows a crack in the membrane; scale bar, 100 nm.

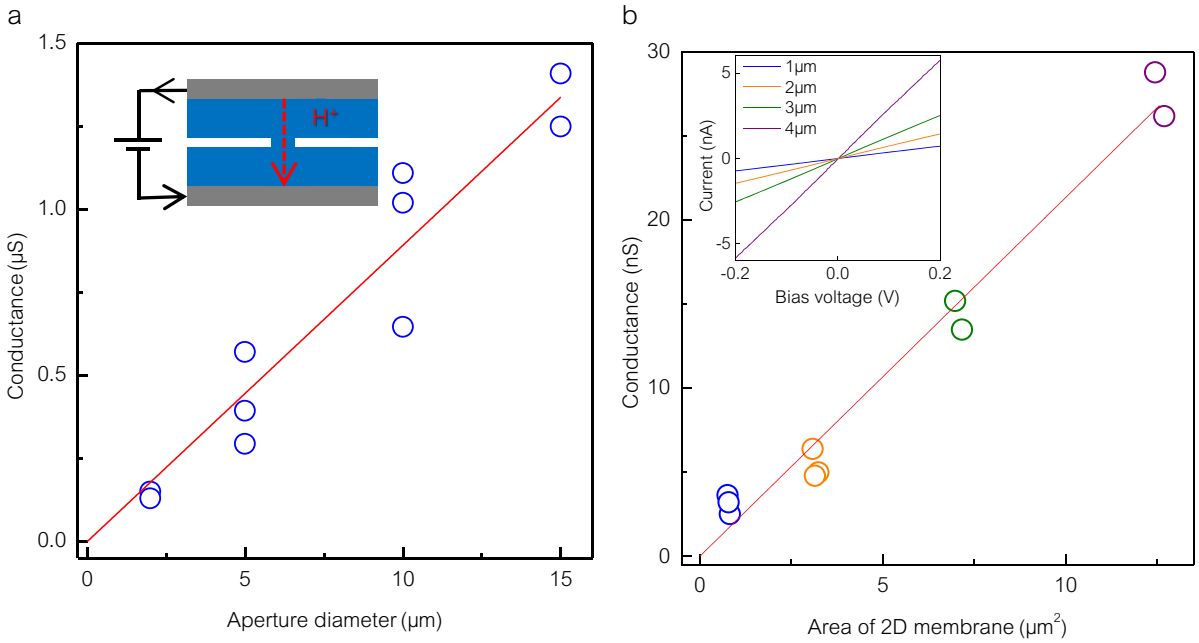

Extended Data Figure 3 | Dependence of proton conductance on aperture size. **a**, A bare-hole device exhibits a linear dependence of σ on the aperture diameter, as expected for this geometry[35]. The inset is a sketch of such a device. **b**, Proton conductance through monolayer hBN scales quadratically with membrane diameter, that is, linearly with membrane area. The inset shows examples of I–V characteristics for four hBN monolayer devices with different D values, from 1 to 4 μm.

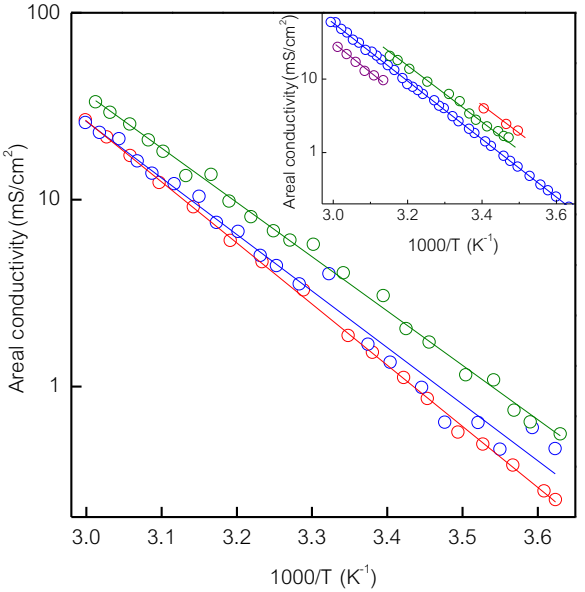

Extended Data Figure 4 | Reproducibility of proton barrier heights for different devices. Activation temperature dependences for three bilayer hBN devices (symbols are the experimental data; lines are the best fits). Inset: equivalent data for four monolayer graphene devices, three of which could be measured only within limited T intervals before they failed. The blue line is the best fit to the Arrhenius-type dependence; the other lines are guides to the eye indicating that all the devices exhibit practically the same E.

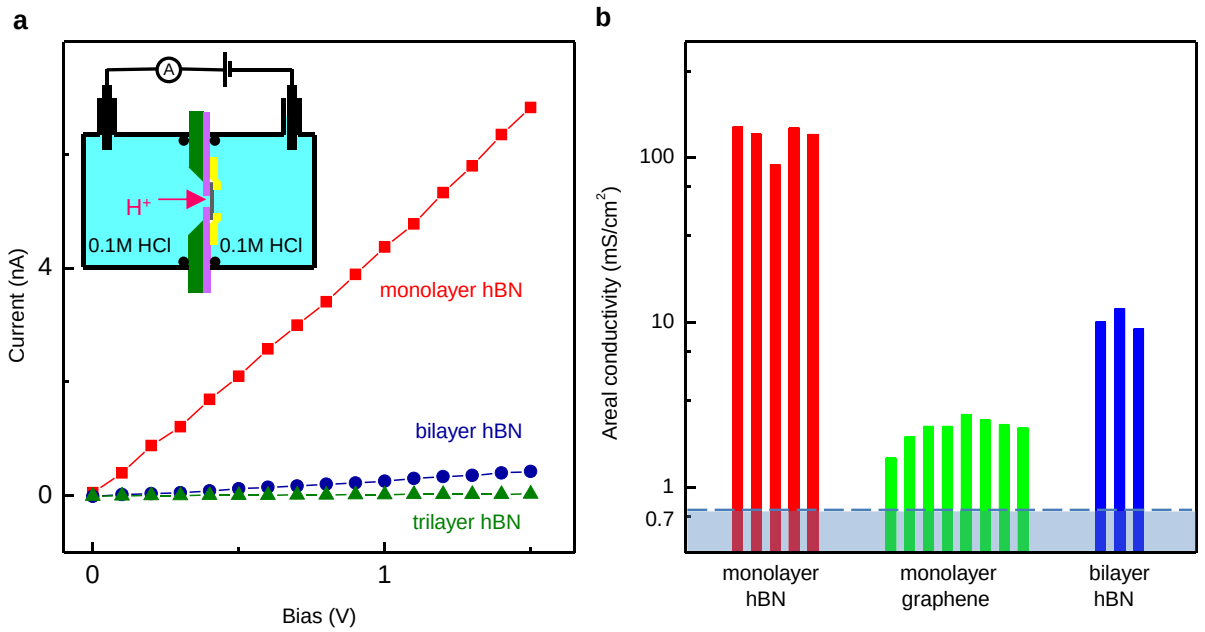

Extended Data Figure 5 | Proton transport through 2D crystals in electrolytes. **a**, Examples of *I*–*V* characteristics for mono-, bi- and trilayer hBN membranes covering an aperture 2 μm in diameter. The inset shows a sketch of the liquid-cell set-up. To match the proton concentration in our Nafion experiments, we used a 0.1 M HCl solution in both containers. An additional polymer seal (yellow) is used to avoid leakage along the 2D crystal/substrate interface[11]. Ag/AgCl electrodes are placed inside each reservoir to measure ionic currents. In the case of trilayer hBN, the measured current falls within the range given by leakage currents. **b**, Histograms for the 2D crystals that exhibited unambiguous proton conductivity in the liquid-cell set-up. Each bar represents a different 2 μm membrane. The shaded area shows our detection limit.

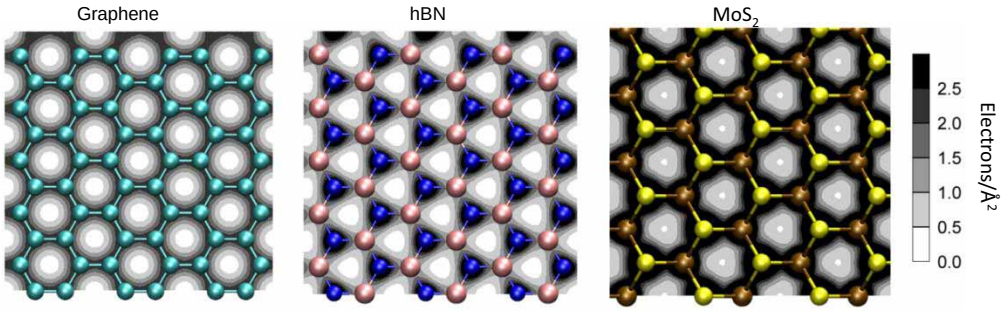

Extended Data Figure 6 | Electron clouds of 2D crystals. Integrated charge densities for graphene, monolayer hBN (nitrogen is indicated by blue balls; boron in pink) and monolayer MoS_2 (S is in yellow; Mo in brown).

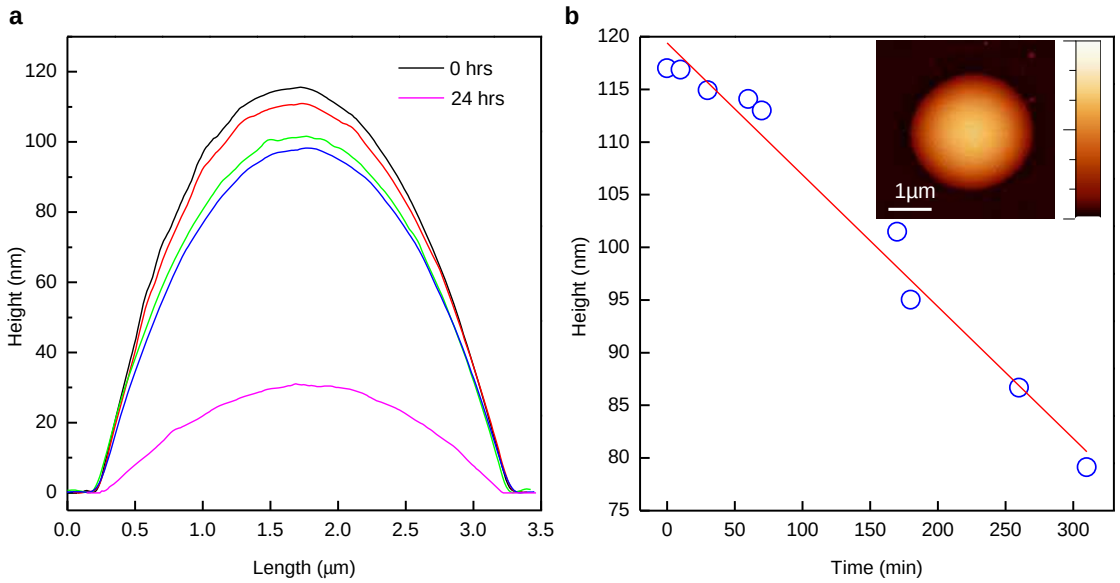

Extended Data Figure 7 | Slow deflation of micro-balloons rules out atomic-scale pinholes. **a**, Height profiles for a typical graphene membrane over 24 h of observation. **b**, Maximum height as a function of time. The inset shows a typical AFM image of a pressurized graphene microcavity (colour scale, 0–130 nm). We measured six graphene membranes and all of them showed the same deflation rates, independently of whether or not Pt was deposited on top. Similar behaviour was observed for hBN monolayers.

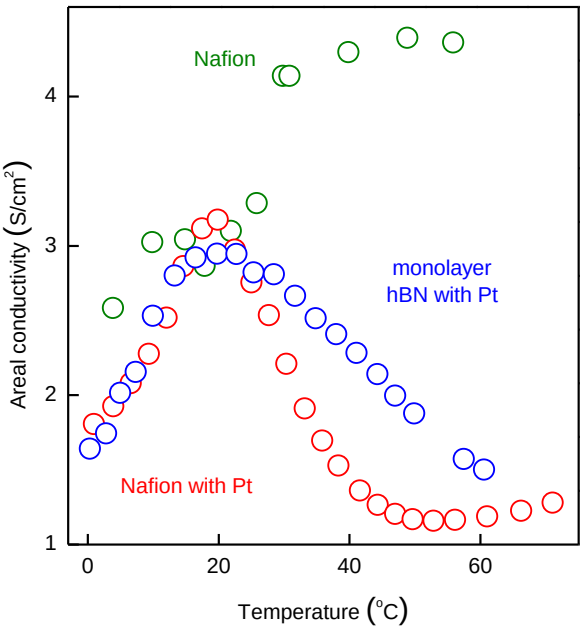

Extended Data Figure 8 | Nafion-limited conductivity for Pt-activated hBN. Temperature dependences for a bare-hole device (constriction with Nafion only), a Nafion/Pt/Nafion device (no 2D membrane present) and a membrane device with catalytically activated monolayer hBN. The nominal conductivity is calculated as the measured conductance S divided by the aperture area A.

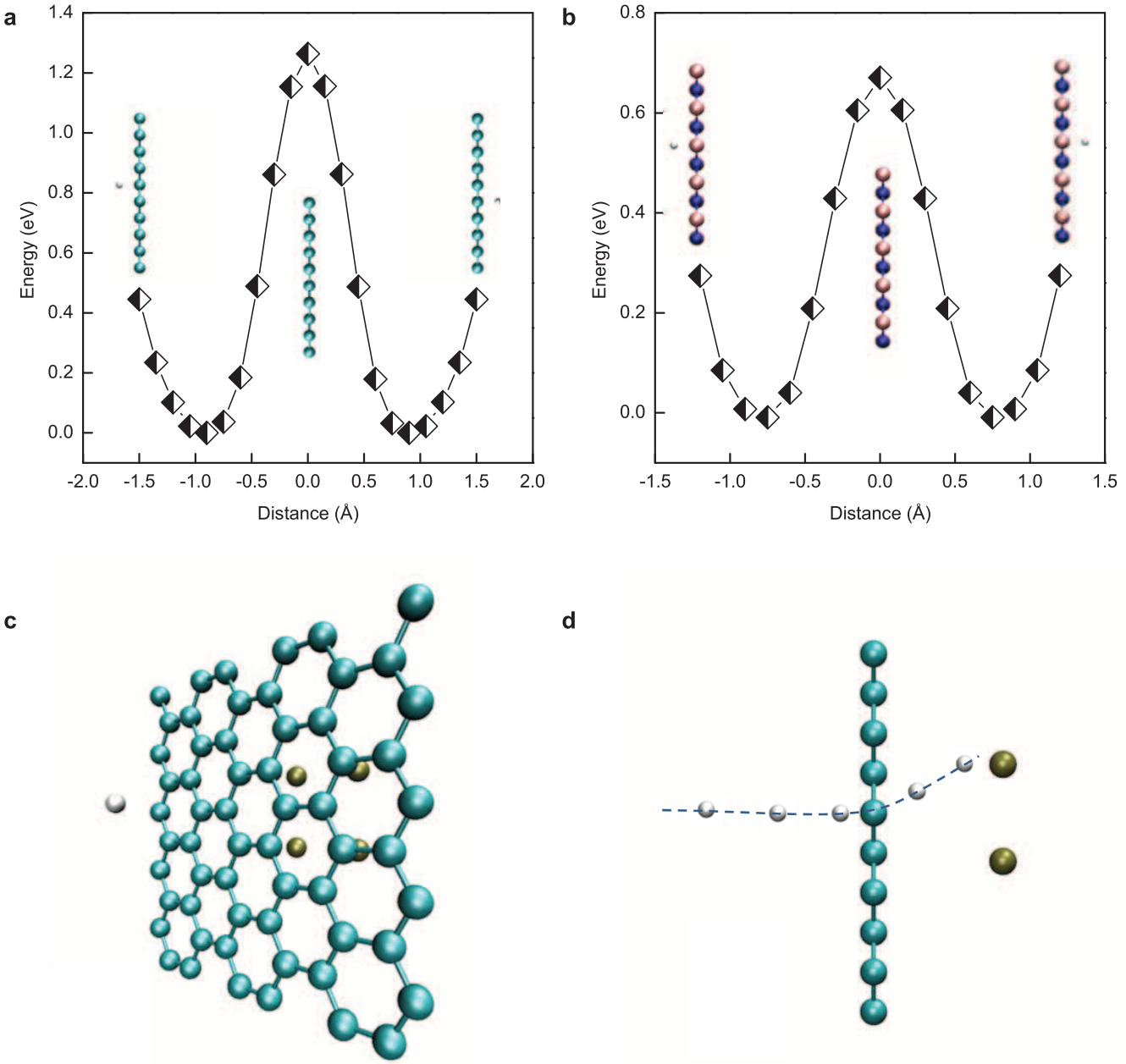

Extended Data Figure 9 | Simulations of proton transport through 2D crystals. a, **b**, Profiles of energy as a function of the distance of the proton to the centre of the hexagonal ring in graphene (**a**) and hBN (**b**), calculated using the CI-NEB method. Carbon atoms are shown in cyan, nitrogen in blue, boron in pink and protons in white. **c**, The influence of catalytic nanoparticles used in the experiment is mimicked by placing four Pt atoms at a distance of 4 Å from the graphene sheet. **d**, Trajectory of protons with an initial kinetic energy of 0.7 eV (the other two Pt atoms cannot be seen because of the perspective). The bent trajectory indicates that the decrease in barrier height is due to interaction of protons with Pt. Carbon atoms are shown in cyan, Pt in ochre and protons in white.

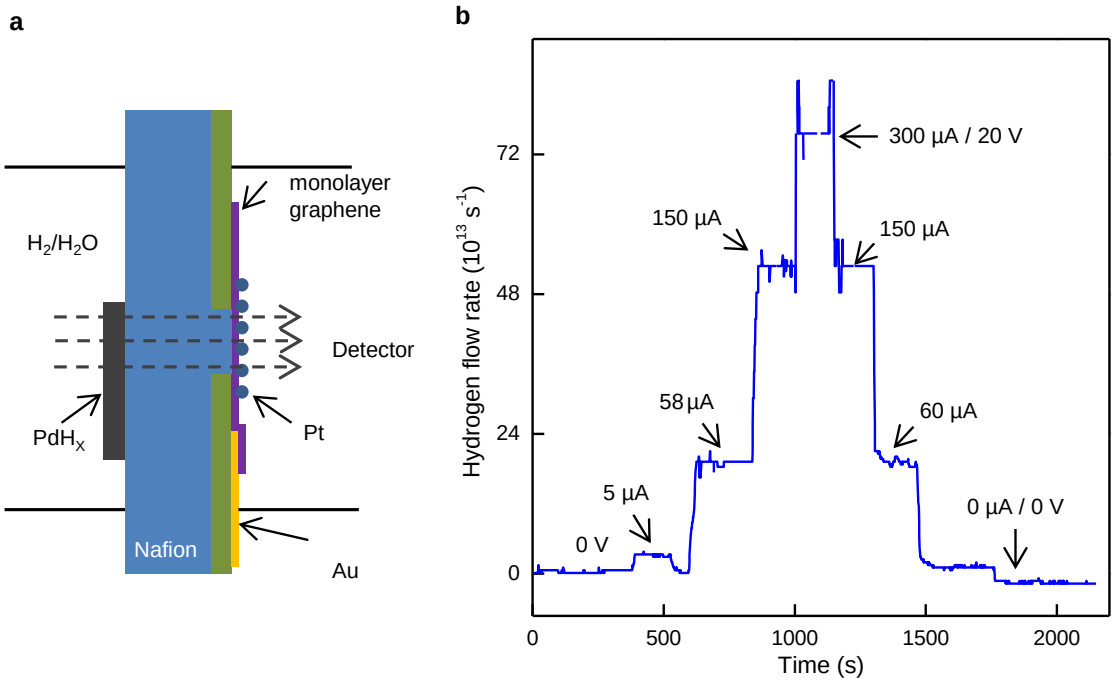

Extended Data Figure 10 | Hydrogen flow detection. **a**, Schematics of our devices for mass spectroscopy measurements. **b**, Example of the observed hydrogen flow rates as a functions of time for different negative biases on the graphene membrane. The voltage was applied in steps and resulted in the current values indicated next to the steps.